AIAA JOURNAL
Vol. 34, No. 6, June 1996

Numerical Investigation of Supersonic Wing-Tip Vortices

Donald P. Rizzetta*
U.S. Air Force Wright Laboratory, Wright–Patterson Air Force Base, Ohio 45433-7913

Steady high-Reynolds-number flowfields about a finite-span rectangular wing mounted upright in a supersonic stream were generated numerically to investigate formation of the tip vortex. Solutions were obtained by integration of the time-dependent three-dimensional compressible Euler and thin-layer laminar and mass-averaged turbulent Navier–Stokes equations. In the turbulent case, a two-equation (k–ϵ) closure model was employed, which included low-Reynolds-number terms and a compressibility correction. Details of the computations are summarized, and a grid resolution study is provided to assess the accuracy of the numerical results. Comparisons are made between solutions of the various governing equations, as well as with experimental data in terms of pressure and Mach-number component distributions in the vortex core.

Nomenclature

c = wing chord, 50.8 mm
k = turbulence kinetic energy
L_2 = L_2 norm of ΔQ
M_x, M_y, M_z = Mach-number components in streamwise, lateral, and vertical directions
N_i, N_j, N_k = number of i, j, k grid points
p = nondimensional static pressure
p_t = nondimensional total pressure
Q = vector of dependent variables
x, y, z = nondimensional Cartesian coordinates in streamwise, lateral, and vertical directions
y_c, z_c = vortex core location
α = angle of attack
ΔQ = change in Q over one time step
$\Delta S_\xi, \Delta S_\eta, \Delta S_\zeta$ = mesh spacing in ξ, η, ζ directions
ϵ = turbulence energy dissipation
ξ, η, ζ = computational coordinates

Subscript

∞ = freestream value

Introduction

THE formation of a vortex at the tip of a finite-span wing and its subsequent propagation into the downstream wake constitute a fundamental aerodynamic phenomenon, which also has considerable practical significance. For supersonic applications, such vortices are commonly produced from the tips of canards, fins, and wings. These vortices may then respond to the associated shock-wave systems present over wings or control surfaces, or within high-speed inlets, resulting in a loss of lift, an increase in drag, poor stability and control, or a decrease in engine performance. Such shock-wave–vortex interactions are in general three-dimensional and unsteady, and, if sufficiently strong, may result in vortex breakdown. Accurate numerical simulation of these occurrences is possible only if the structure of the tip vortex has been correctly reproduced.

Although few supersonic calculations exist, a number of computations have been performed to simulate subsonic wing-tip vortices.[1–3] Because these vortices evolve from a three-dimensional separation of viscous layers near the wing surface, which roll up and are convected downstream, the studies have focused on solutions of the Navier–Stokes equations. For practical applications, however, it has been shown that wing-tip vortices may be generated numerically by Euler solutions.[4] Although inviscid results are useful, they cannot properly describe the detailed mechanisms of vorticity transport from viscous surface layers into a concentrated vortex. The calculations of Dacles-Mariani et al.[3] have shown that the flowfield immediately surrounding the vortex core is extremely sensitive to grid resolution, turbulence modeling, and numerical dissipation.

Several computational investigations have been conducted to simulate the interaction between a streamwise vortex and an oblique shock wave.[5–7] When the vortex forms at the tip of a finite-span wing, it has not been possible to numerically duplicate all of the features of the flowfield that occurred experimentally.[8–10] The comprehensive computations of Rizzetta[7] failed to predict the vortex breakdown that was often observed. It was believed that the vortex core might not have been adequately described, but because no detailed measurements within the vortex core region were available, the reason for this discrepancy was unknown.

Because of the small number of quantitative measurements of supersonic tip vortices that are available for numerical validation,[11–13] the recent work of Smart et al.[14] was performed to describe the flowfield through the core of vortices produced at the tip of a finite-span wing at angle of attack. Distributions of pressure and Mach-number components in three directions were determined by a unique technique consisting of direct measurements and numerical calibration. The configuration is depicted schematically in Fig. 1 and consists of air flow at a freestream Mach number of 2.49 and chord Reynolds number of 2.17×10^6 through a wind tunnel with a square cross-section measuring 381.0 mm on a side. A streamwise vortex is generated at the tip of a rectangular wing, which has sharp leading and trailing edges, a blunt tip with sharp edges, and a symmetric diamond cross-sectional shape. The wing has a span of 165.1 mm, a chord of 50.8 mm, a maximum thickness of 7.1 mm, and leading- and trailing-edge included angles of 16.0 deg. A Cartesian coordinate system was oriented with its vertical (z) axis running through the center of the wing cross section, and with its origin at the wing tip (see Fig. 1). The wing was mounted upright on the floor of the wind tunnel and rotated about the z axis to angles of attack α, which were taken to be positive when the leading edge was located at $y > 0$. In this way, a tip vortex was produced, whose strength could be controlled by varying the angle of attack.

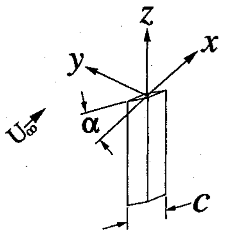

Fig. 1 Vertical wing configuration.

Received June 6, 1995; presented as Paper 95-2282 at the AIAA 26th Fluid Dynamics Conference, San Diego, CA, June 19–22, 1995; revision received Nov. 17, 1995; accepted for publication Nov. 22, 1995. This paper is declared a work of the U.S. Government and is not subject to copyright protection in the United States.

*Research Aerospace Engineer, Computational Fluid Dynamics Research Branch, Aeromechanics Division. Associate Fellow AIAA.

Table 1 Computational mesh parameters

Mesh designation	Mesh size	$\Delta S_{\xi\,\min}$	$\Delta S_{\eta\,\min}$	$\Delta S_{\zeta\,\min}$
Coarse	128 × 59 × 54	6.04×10^{-3}	9.94×10^{-5}	1.10×10^{-4}
Medium	192 × 88 × 81	3.42×10^{-3}	7.45×10^{-5}	7.53×10^{-5}
Fine	255 × 117 × 107	3.00×10^{-3}	4.97×10^{-5}	5.01×10^{-5}

The purpose of the present investigation is to simulate numerically the wing-tip vortex that was considered experimentally in Ref. 14. Solutions were obtained to the compressible three-dimensional Euler and mass-averaged thin-layer laminar and turbulent Navier–Stokes equations. In the turbulent case, a two-equation (k–ϵ) closure model was employed, which included low-Reynolds-number terms and a compressibility correction. The numerical procedure is summarized, details of the computations are presented, and grid studies are provided to assess the accuracy of the solutions. Numerical results are computed for wing angles of attack of $\alpha = 5.0$ and 10.0 deg, corresponding to the experimental conditions. Comparisons are made between solutions of the various governing equations, as well as with experimental data in terms of pressure and Mach-number component distributions in the vortex core.

Governing Equations

The governing equations were taken to be the unsteady compressible three-dimensional Euler and thin-layer laminar and mass-averaged turbulent Navier–Stokes equations. Effects of turbulence were allowed for by specifying a turbulent Prandtl number of 0.90, and by incorporating a two-equation model for the turbulence kinetic energy k and the turbulence dissipation rate ϵ. The k–ϵ equations are essentially identical to those developed by Jones and Launder,[15,16] and include low-Reynolds-number terms to improve near-wall modeling. In addition, a compressibility correction[17] is utilized to represent supersonic flows more adequately. These equations have been successfully applied to simulate a variety of complex turbulent flowfields, including supersonic slot injection,[18] cylinder juncture flows,[19] and jet expulsion.[20]

The complete description of the governing equations, including that for the turbulence model, appears in Ref. 21. A perfect gas was assumed, and for viscous calculations the Sutherland law for the molecular viscosity coefficient and Stokes' hypothesis for the bulk viscosity coefficient were employed.

Numerical Procedure

Solutions to the governing equations were obtained numerically using the implicit approximately factored finite-difference algorithm of Beam and Warming,[22] which has evolved as an efficient tool for generating solutions to a wide variety of complex fluid flow problems. First-order Euler implicit time differencing was employed along with second-order accurate central-difference approximations for all spatial derivatives. Common forms of both implicit and explicit nonlinear artificial dissipation[23] were utilized to augment stability, with the pressure-gradient parameter given according to Swanson and Turkel.[24] Usual values of user-defined damping coefficients were assigned, and for viscous calculations, the dissipation was scaled by the square of the local velocity magnitude so that it essentially vanished in regions adjacent to solid surfaces. Efficiency was enhanced by solving the implicit portion of the factorized equations in diagonalized form.[25]

For turbulent computations, the k–ϵ equations were temporally decoupled from the mean-flow equations by lagging their values by one time step from the other dependent variables. In addition, k and ϵ were implicitly uncoupled from each other by also evaluating the vector source term explicitly from the previous time step. This technique has been shown to be effective for a number practical flow applications.[19,20]

The aforementioned features of the numerical algorithm are embodied in an existing fully vectorized time-accurate three-dimensional computer code. This code has proven to be reliable for a number of both steady and unsteady fluid flow problems, including the simulation of supersonic flows with shock waves,[19,26] flows over delta wings with leading-edge vortices,[27–30] vortex breakdown,[29,30] and oblique shock-wave–vortex interactions.[7]

Computational Meshes

The computational mesh about the finite-span wing consisted of an H–H topology, which was generated by constructing a two-dimensional grid in the ξ–η plane, where the ξ direction is streamwise, the η direction lateral, and the ζ direction vertical. Mesh points were distributed along the lateral surfaces of the wing and obtained in the field by solution of elliptic equations[31] to ensure grid quality, smoothness, and orthogonality of grid lines. Spanwise boundaries of the computational domain coincided with the location of the wind-tunnel sidewalls. The two-dimensional grid was then distributed in the vertical direction according to the one-dimensional stretching function of Vinokur,[32] where the top and bottom boundaries of the domain corresponded to the ceiling and floor of the wind tunnel, respectively.

Downstream of the wing trailing edge, grid-point clustering in the spanwise and vertical directions was maintained along a trajectory that approximated the path of the vortex core. The entire three-dimensional grid was then elliptically smoothed.[31] Preliminary coarse-grid computations were performed, a more exact core trajectory was determined, and the downstream portion of the grid was regenerated and smoothed to achieve the final mesh-point distribution.

The primary grids for these computations consisted of 255 × 117 × 107 points in the (ξ, η, ζ) directions. Of these, 100 ξ-grid lines were employed over the chord of the wing, and 10 ξ-grid lines were located upstream of the wing leading edge. Grid-point clustering was enforced in the streamwise (ξ) direction at the wing leading and trailing edges, in the lateral (η) direction at the wing surfaces, and in the vertical (ζ) direction at the wing tip. With this grid structure, fictitious mesh points were employed in the interior of the wing surface. These points emerged from the tip of the wing at $z = 0$ to describe the upper portion of the flowfield directly above the wing tip. Because the domain lateral and vertical boundaries were constrained by the wind-tunnel wall positions, it was necessary to generate separate grids for each value of the angle of attack α.

For the purpose of studying effects of grid resolution, a coarse computational mesh was obtained by removing every other point in each coordinate direction from the 255 × 117 × 107 grid. An intermediate mesh was also constructed, maintaining the same regions of clustering and stretching. Parameters for these grids corresponding to $\alpha = 10.0$ deg may be found in Table 1.

Identical meshes were employed to obtain solutions to each set of governing equations. As a result, in the inviscid case the grid spacing at the wing surface is much finer than would normally be required for adequate resolution. It is considered significant, however, that all solutions were obtained on the same grid to eliminate as much as possible any numerical differences among the results.

Boundary Conditions

Inflow conditions at the upstream computational boundary were taken as freestream. Details of the values prescribed for k_∞ and ϵ_∞ may be found in Ref. 21. The downstream boundary was located slightly aft of the experimental data-measuring position, so that the numerical solution at the measurement station was uninfluenced by the downstream boundary. Second-order accurate extrapolation from the interior region was employed to establish values of all dependent variables at the downstream outflow surface.

Inviscid solid-wall conditions were enforced at the upper, lower, and lateral domain boundaries, corresponding to the wind-tunnel walls, for solutions to both the Euler and Navier–Stokes equations.

In the viscous case, this precluded the necessity of fine grid resolution normal to the domain boundaries, thus minimizing the demand for computational resources, but still allowed for the confinement effect of the solid tunnel walls. On the wing surface, inviscid solid-wall conditions were utilized in Euler computations. For the Navier–Stokes calculations, the no-slip condition, an adiabatic wall, and a vanishing normal pressure gradient were employed, and in the turbulent case homogeneous conditions for k and ϵ were specified.

Details of the Computations

Steady-state solutions to the governing equations were obtained numerically by marching in time via the previously described method. For each set of equations, steady two-dimensional results at each angle of attack were first computed about the wing cross-sectional shape in the ξ–η plane. These planar solutions were then distributed along the vertical span of the wing to initialize the three-dimensional flowfields. Coarse-grid three-dimensional solutions were obtained and interpolated onto fine grids. Final steady-state Euler results were subsequently achieved in approximately 2000 time steps, for which convergence was evidenced by $L_2 < 4.0 \times 10^{-18}$, where

$$L_2 \equiv \frac{1}{N_i N_j N_k} \sum_i \sum_j \sum_k (\Delta Q_{ijk} \ \Delta Q_{ijk})^{\frac{1}{2}}$$

Corresponding fine-grid laminar Navier–Stokes computations required 5000 time steps, resulting in $L_2 < 2.0 \times 10^{-7}$. For the k–ϵ equations, steady-state solutions were attained after 10,000 time steps, for which $L_2 < 6.0 \times 10^{-7}$. Local time stepping was employed for all calculations. In addition to the L_2 norm, the surface pressure and skin-friction (in viscous cases) distributions on the wing surface were monitored, as well as the vortex profile at the downstream boundary to ascertain convergence. All of the computations reported here were performed on a Cray Y-MP C916/16256, for which the data-processing rate was approximately 3.9×10^{-6} (CPU s)/(time step)(grid point) for the Euler equations, 7.8×10^{-6} for the laminar thin-layer Navier–Stokes equations, and 1.7×10^{-5} for the k–ϵ set.

Quality of the Solutions

Experimental measurements with both $\alpha = 5.0$ and 10.0 deg were conducted at a streamwise location of 2.25 chords downstream from the wing trailing edge. At each angle of attack, the lateral position of these measurements was taken to be that for which the pitot pressure was a minimum. Surveys were then performed in the vertical direction to ascertain properties of the vortex core flow. Corresponding numerical flowfield information was extracted in a similar manner. Note that because the vortex core location (y_c, z_c) that eventuated from each solution was not constant, comparisons are made at spanwise positions that vary in space for each numerical result, but are fixed relative to the vortex core. Table 2 indicates the variation of the vortex core location among the cases.

Solutions to all sets of equations on the three different grid systems are displayed in Fig. 2 in terms of the nondimensional total pressure distribution through the vortex core at the data-measuring station. Little difference is observed between the medium- and fine-grid solutions in each case, except near the top of the vortex ($z \approx -0.02$), where changes in gradients are large. The location and magnitude of the point of minimum total pressure, representing the vortex center, appears to be well resolved on the medium grid, thus lending confidence to the fine-grid result.

Table 2 Location of the vortex core

α, deg	Case	y_c	z_c
5.0	Euler	−0.048	−0.104
	Laminar N–S	−0.048	−0.093
	k–ϵ N–S	−0.040	−0.093
	Experiment	−0.060	−0.016
10.0	Euler	−0.065	−0.118
	Laminar N–S	−0.067	−0.115
	k–ϵ N–S	−0.062	−0.118
	Experiment	−0.065	−0.063

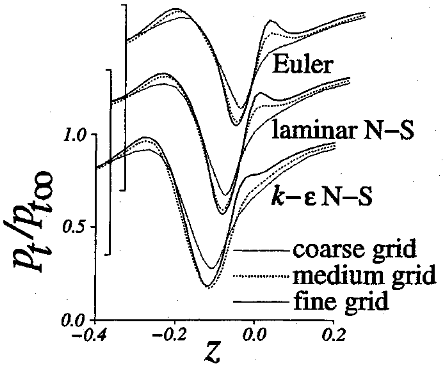

Fig. 2 Effect of grid resolution on total-pressure distributions through the vortex core for $\alpha = 10.0$ deg.

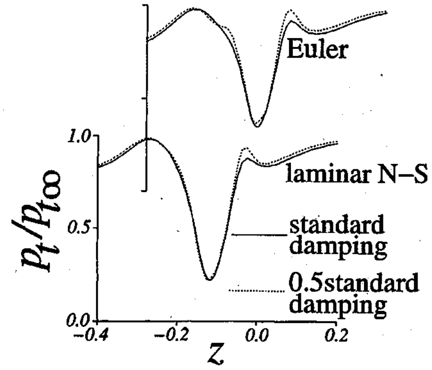

Fig. 3 Effect of damping coefficient on total-pressure distributions through the vortex core for $\alpha = 10.0$ deg.

For the Euler and laminar Navier–Stokes equations, the implicit and explicit nonlinear damping coefficients were reduced to one-half their standard values and solutions were obtained on the fine computational mesh to determine the effect of artificial dissipation upon the computations. Total-pressure distributions of these calculations appear in Fig. 3. Decreased damping is seen to have only a slight influence on the solutions except in the high-change-of-gradient region ($z \approx -0.02$). Calculations were slightly less stable when the lower damping coefficients were employed. Because of the additional computational effort required by the k–ϵ equations, no solutions with reduced values of damping were attempted for that set.

To assess limitations of the thin-layer approximation, a solution to the full laminar Navier–Stokes equations was obtained on the fine computational mesh. A comparison between this calculation and the corresponding thin-layer result that was made in Ref. 21 confirmed the validity of the thin-layer assumption for the vortical flow.

Features of the Flowfield

All the remaining discussion of numerical results will pertain to fine-grid solutions employing standard values of the damping coefficients. Features of the flowfield obtained with the k–ϵ equations for $\alpha = 10.0$ deg are illustrated in Figs. 4–6. Mach-number contours in an x–y plane and surface pressure coefficient contours near the inboard wing tip are shown in Fig. 4. The shock wave emanating from the leading edge and the expansion about the lateral midchord apex are evident in the Mach-number contours, as are the boundary-layer region and downstream wake. Pressure contours show the expansion of the flow over the inboard edge of the wing tip.

Particle paths of the vortex core flow and contours of constant total pressure at several streamwise stations appear in Fig. 5. The stations represented in the figure are at the 50, 75, and 100% chord locations on the wing surface, and at 0.5, 1.0, and 2.25 chord lengths downstream of the trailing edge in the wake. A close-up view of the trailing-edge region is seen in Fig. 6. The formation of two discrete vortices, created by expansion of the flow about the wing

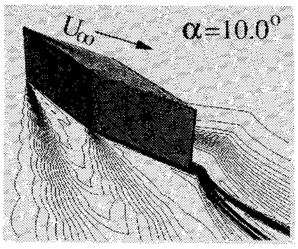

Fig. 4 Mach-number contours in an x–y plane and pressure-coefficient contours on the inboard wing surface near the tip from the k–ϵ solution for α = 10.0 deg.

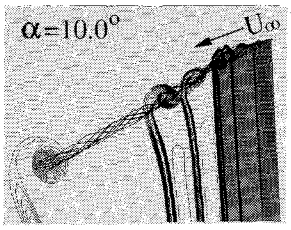

Fig. 5 Crossplane total-pressure contours at the wing tip and in the downstream region from the k–ϵ solution for α = 10.0 deg.

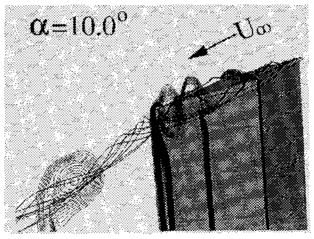

Fig. 6 Crossplane total-pressure contours at the wing tip and in the trailing-edge region from the k–ϵ solution for α = 10.0 deg.

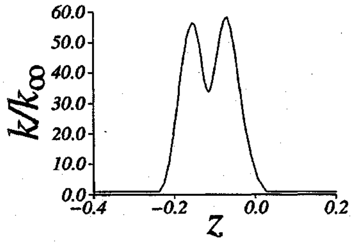

Fig. 7 Turbulent kinetic energy distribution through the vortex core at the data-measuring station for α = 10.0 deg.

tip and leading edge, and separation from each of the sharp edges of the tip, is apparent near midchord. At the 75% chord location these vortices are quite well defined. The tapering of the diamond cross-sectional geometry into a sharp trailing edge helps bring the vortices into close proximity with each other downstream, where they merge and amalgamate into a single vortex aft of the trailing edge. A single coherent, nearly symmetric structure can be observed at the downstream location (see Fig. 5).

A distribution of the vortex-core turbulence kinetic energy at the data measurement station is displayed in Fig. 7. The maxima of the nearly symmetric distribution represent turbulence energy that formed in the boundary layers along the lateral surfaces of the wing and subsequently was entrained into the vortex-core flow of the downstream wake region. At the vortex center, the energy is seen to be only about one-half the peak values.

Comparison with Experiment

A visual comparison between the computed magnitude of the density gradient for the k–ϵ solution and an experimental laser-light-sheet image when $\alpha = 10.0$ deg is provided in Fig. 8. These representations correspond to the flowfield at a location 4.0 chords aft of the wing trailing edge, and viewed looking downstream, but seen from an angle rotated 45.0 deg with respect to the axial direction. To obtain the k–ϵ result at this location, the solution domain had to be extended downstream from the data-measuring station using a $155 \times 117 \times 107$ grid. Care was taken to scale the respective images in an identical manner so that physical lengths were depicted identically in each frame. The purpose of the figure is to compare the size and shape of the computed vortex with its experimental counterpart. Visually, these properties appear to agree reasonably well.

Nondimensional total-pressure distributions through the vortex core at the data-measuring station are given in Fig. 9. Numerical

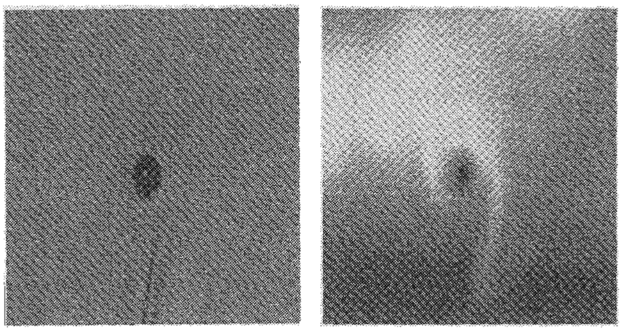

Computation Experiment

Fig. 8 Flowfield visualization in a crossplane downstream from the data-measuring station of the k–ϵ solution and experimental data for α = 10.0 deg.

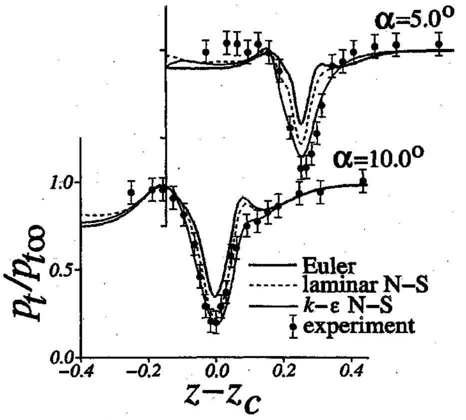

Fig. 9 Total-pressure distributions through the vortex core.

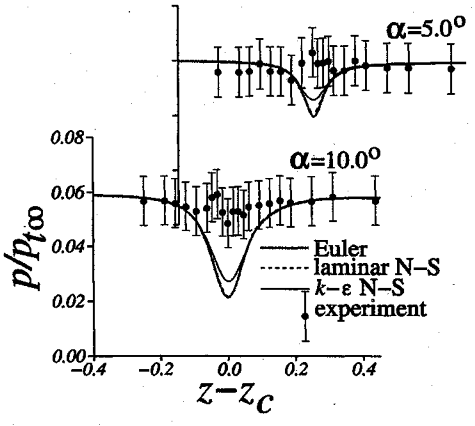

Fig. 10 Static-pressure distributions through the vortex core.

solutions to each set of equations are presented, as well as experimental data. Error bars resulting from an accuracy analysis of the measurements[14] are included with the data. For this and the remaining figures, the origin of the vertical (z) axis has been translated to the vortex center of each distribution so that profiles can be compared spatially with respect to the vortex core. It can be noted from Table 2 that all numerical results indicate a vortex core that lies somewhat below the experimental location. The Euler solution appreciably underpredicts both the size and the strength of the vortex. And though the laminar calculation compares better with the experiment, the k–ϵ result is clearly superior, particularly near the top of the vortex ($z - z_c \approx 0.05$).

Corresponding static-pressure levels may be found in Fig. 10. Although the pressure varies only slightly from the freestream value ($p_\infty/p_{t\infty} = 0.0594$) through the core, both the Euler and the laminar Navier–Stokes computations produce a greater pressure reduction than the k–ϵ equations. Surprisingly, no decrease

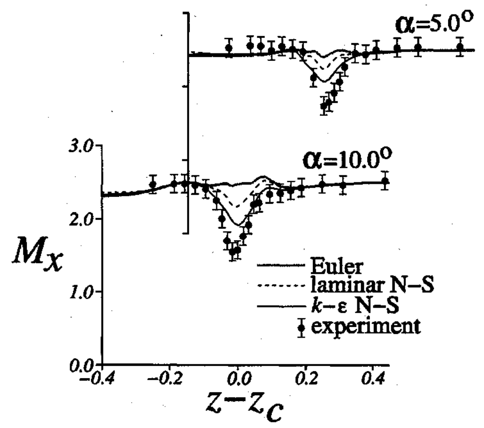

Fig. 11 Streamwise-Mach-number distributions through the vortex core.

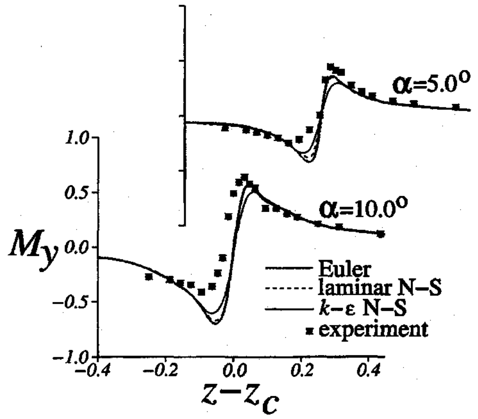

Fig. 12 Lateral-Mach-number distributions through the vortex core.

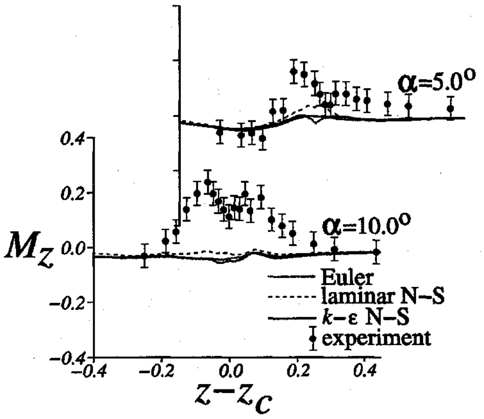

Fig. 13 Vertical-Mach-number distributions through the vortex core.

of the core pressure is evident in the data. Subsequent experimental measurements taken at slightly different flow conditions,[33] however, did indicate a static-pressure reduction in the vortex core.

Vortex-core streamwise Mach-number components appear in Fig. 11. Here the Euler solution produces no core Mach-number deficit, the laminar calculation predicts a modest deficit, and the k–ϵ result most resembles the experiment. Lateral-Mach-number distributions are shown in Fig. 12. The numerical results appear more symmetric than the experimental data. The Euler and laminar Navier–Stokes solutions are quite similar, having greater local maxima and minima than the k–ϵ calculation. Note that the maximum variation in this component across the vortex core for the k–ϵ solution is comparable to that of the measurements. Figure 13 compares vertical-Mach-number distributions. Even though the magnitude of this component is small relative to M_x, all the computations predict a negligible value of M_z, as opposed to the more significant level in the experimental data.

Summary and Conclusions

High-Reynolds-number flowfields about a finite-span rectangular wing mounted upright in a supersonic stream were generated numerically to investigate the formation of the tip vortex. Two angles of attack were considered, corresponding to vortices of different strengths. In each case, solutions were obtained to the three-dimensional compressible Euler and mass-averaged thin-layer laminar and turbulent Navier–Stokes equations. For the turbulent calculations, a two-equation (k–ϵ) closure model was employed, which included low-Reynolds-number terms and a compressibility correction.

Grid studies were performed for all sets of equations, indicating that on the finest mesh, the resolution was adequate to describe the principal features of the flow. An examination of explicitly added artificial damping demonstrated that the computations were not appreciably degraded by numerical dissipation. Comparisons were made between solutions of the various governing equations and with experimental data in terms of pressure and Mach-number component distributions in the vortex core. These comparisons revealed that the k–ϵ results most closely reproduced the test measurements.

Total-pressure distributions for the vortex core flow were not described very well by the Euler equations. This circumstance is unlike the simulation of leading-edge vortices, where inviscid equations have successfully accounted for total-pressure losses of flows past delta wings with sharp edges at angle of attack.[34] In the finite-span wing configuration, vortices are produced at the sharp edges of the wing tip, similarly to the delta-wing situation. As the vortices merge downstream, however, boundary-layer flow from the surfaces is entrained into the core, resulting in a region of fluid that has incurred an additional loss of total pressure. The Euler equations cannot simulate this occurrence. By contrast, the primary vortex emanating from a delta wing with sharp leading edges contains little fluid that has been influenced by viscous dissipation. Use of the laminar Navier–Stokes equations accounts for the boundary layers on the wing surfaces, but neglects turbulent effects in high-Reynolds-number flowfields.

The fact that the k–ϵ equations adequately duplicate the total-pressure distribution through the vortex core implies that the model may properly allow for global turbulent losses. Deficiencies in accurate simulation of the static pressure and components of the Mach number, however, indicate that the losses are not partitioned correctly among the various energy modes. This must be considered a limitation of the turbulence model for wing-tip vortex flows.

Although certain inadequacies in the turbulence model are evident, it is notable that a deficit in the streamwise Mach number of the vortex core has been predicted by the k–ϵ equations. This structure is believed to be a key factor contributing to the observed breakdown of the vortex upon its subsequent interaction with an oblique shock wave.[8–10,35] Computations that failed to allow for the deficit[5,7] have been unable to numerically reproduce oblique shock-wave-induced vortex breakdown.

Acknowledgments

Computational resources for the work presented here were supported in part by a grant of high-performance computing (HPC) time from the Department of Defense HPC Shared Resource Center, U.S. Army Corps of Engineers Waterways Experiment Station, Vicksburg, MS. The author is indebted to I. M. Kalkhoran and M. K. Smart for their assistance and cooperation in supplying details and results of the experiment. A number of helpful conversations with R. E. Gordnier are gratefully acknowledged.

References

[1] Mansour, N. N., "Computation of the Tip Vortex off a Low-Aspect-Ratio Wing," *AIAA Journal*, Vol. 23, No. 8, 1985, pp. 1143–1149.

[2] Srinivasan, G. R., McCroskey, W. J., Baeder, J. D., and Edwards, T. A., "Numerical Simulation of Tip Vortices of Wings in Subsonic and Transonic Flows," *AIAA Journal*, Vol. 26, No. 10, 1988, pp. 1153–1162.

[3] Dacles-Mariani, J., Rogers, S., Kwak, D., Zilliac, G., and Chow, J., "A Computational Study of Wingtip Vortex Flowfield," AIAA Paper 93-3010, July 1993.

[4] Rizzi, A., "Damped Euler Equation Method to Compute Transonic Flow Around Wing–Body Combinations," *AIAA Journal*, Vol. 20, No. 10, 1982, pp. 1321–1328.

[5] Corpening, G., and Anderson, J. D., "Numerical Solutions to Three-Dimensional Shock Wave/Vortex Interaction at Hypersonic Speeds," AIAA Paper 89-0674, Jan. 1989.

[6] Kandil, O. A., Kandil, H. A., and Liu, C. H., "Supersonic Quasi-Axisymmetric Vortex Breakdown," AIAA Paper 91-3311, Sept. 1991.

[7] Rizzetta, D. P., "Numerical Simulation of Oblique Shock-Wave/Vortex Interaction," *AIAA Journal*, Vol. 33, No. 8, 1995, pp. 1441–1446.

[8] Kalkhoran, I. M., Sforza, P. M., and Wang, F. Y., "Experimental Study of Shock–Vortex Interaction in a Mach 3 Stream," AIAA Paper 91-3270, Sept. 1991.

[9] Kalkhoran, I. M., "Vortex–Distortion During Vortex-Surface Interaction in a Mach 3 Stream," *AIAA Journal*, Vol. 32, No. 1, 1994, pp. 123–129.

[10] Kalkhoran, I. M., and Sforza, P. M., "Airfoil Pressure Measurements During Oblique Shock Wave-Vortex Interaction in a Mach 3 Stream," *AIAA Journal*, Vol. 32, No. 4, 1994, pp. 783–788.

[11] Adamson, D., and Boatright, W. B., "Investigation of Downwash, Sidewash, and Mach Number Distribution Behind a Rectangular Wing at Mach 2.41," NACA Rept. 1340, July 1950.

[12] Davis, T., "The Measurement of Downwash and Sidewash Behind a Rectangular Wing at a Mach Number of 1.6," *Journal of the Aeronautical Sciences*, Vol. 19, No. 5, 1952, pp. 329–332, 340.

[13] Wang, F. Y., and Sforza, P. M., "An Exploratory Wind Tunnel Study of Supersonic Tip Vortices," AIAA Paper 93-2923, July 1993.

[14] Smart, M. K., Kalkhoran, I. M., and Bentson, J., "Measurements of Supersonic Wing Tip Vortices," AIAA Paper 94-2576, June 1994.

[15] Jones, W. P., and Launder, B. E., "The Prediction of Laminarization with a Two-Equation Model of Turbulence," *International Journal of Heat and Mass Transfer*, Vol. 15, No. 2, 1972, pp. 301–314.

[16] Jones, W. P., and Launder, B. E., "The Calculation of Low-Reynolds-Number Phenomena with a Two-Equation Model of Turbulence," *International Journal of Heat and Mass Transfer*, Vol. 16, No. 6, 1973, pp. 1119–1130.

[17] Sarkar, S., Erlebacher, G., Hussaini, M. Y., and Kreiss, H. O., "The Analysis and Modelling of Dilatational Terms in Compressible Turbulence," *Journal of Fluid Mechanics*, Vol. 227, 1991, pp. 473–493.

[18] Rizzetta, D. P., "Numerical Simulation of Slot Injection into a Turbulent Supersonic Stream," *AIAA Journal*, Vol. 30, No. 10, 1992, pp. 2434–2439.

[19] Rizzetta, D. P., "Numerical Simulation of Turbulent Cylinder Juncture Flowfields," *AIAA Journal*, Vol. 32, No. 6, 1994, pp. 1113–1119.

[20] Mundy, J. A., Rizzetta, D. P., and Melville, R. B., "Numerical Simulation of the Jet Produced by an Internal Aircraft Explosion," *Journal of Aircraft*, Vol. 32, No. 2, 1995, pp. 370–376.

[21] Rizzetta, D. P., "Numerical Investigation of Supersonic Wing-Tip Vortices," AIAA Paper 95-2282, June 1995.

[22] Beam, R., and Warming, R., "An Implicit Factored Scheme for the Compressible Navier–Stokes Equations," *AIAA Journal*, Vol. 16, No. 4, 1978, pp. 393–402.

[23] Jameson, A., Schmidt, W., and Turkel, E., "Numerical Solutions of the Euler Equations by Finite Volume Methods Using Runge–Kutta Time Stepping Schemes," AIAA Paper 81-1259, June 1981.

[24] Swanson, R. C., and Turkel, E., "On Central-Differencing and Upwind Schemes," *Journal of Computational Physics*, Vol. 101, No. 2, 1992, pp. 292–306.

[25] Pulliam, T. H., and Chaussee, D. S., "A Diagonal Form of an Implicit Approximate-Factorization Algorithm," *Journal of Computational Physics*, Vol. 39, No. 2, 1981, pp. 347–363.

[26] Webster, W. P., and Shang, J. S., "Thin-Layer Full Navier–Stokes Simulations over a Supersonic Delta Wing," *AIAA Journal*, Vol. 29, No. 9, 1991, pp. 1363–1369.

[27] Gordnier, R. E., and Visbal, M. R., "Numerical Simulation of Delta-Wing Roll," AIAA Paper 93-0554, Jan. 1993.

[28] Gordnier, R. E., "Computation of Delta-Wing Roll Maneuvers," AIAA Paper 93-2975, July 1993.

[29] Visbal, M. R., "Computational Study of Vortex Breakdown on a Pitching Delta Wing," AIAA Paper 93-2974, July 1993.

[30] Visbal, M. R., "Onset of Vortex Breakdown Above a Pitching Delta Wing," *AIAA Journal*, Vol. 32, No. 8, 1994, pp. 1568–1575.

[31] Steinbrenner, J. P., Chawner, J. P., and Fouts, C. L., "The GRIDGEN 3D Multiple Block Grid Generation System, Volume II: User's Manual," Flight Dynamics Lab., Wright Research and Development Center, WRDC-TR-90-3022, Wright–Patterson AFB, OH, Feb. 1991.

[32] Vinokur, M., "One-Dimensional Stretching Functions for Finite-Difference Calculations," *Journal of Computational Physics*, Vol. 50, No. 2, 1983, pp. 215–234.

[33] Smart, M. K., Kalkhoran, I. M., and Bentson, J., "Measurements of Supersonic Wing Tip Vortices," *AIAA Journal*, Vol. 33, No. 10, 1995, pp. 1761–1768.

[34] Powell, K. G., Murman, E. M., Perez, E. S., and Baron, J. R., "Total Pressure Loss in Vortical Solutions of the Conical Euler Equations," *AIAA Journal*, Vol. 25, No. 3, 1987, pp. 360–368.

[35] Smart, M. K., and Kalkhoran, I. M., "The Effect of Shock Strength on Oblique Shock Wave–Vortex Interaction," AIAA Paper 95-0098, Jan. 1995.